# High-throughput design of complex oxides as isothermal, redox-activated CO<sub>2</sub> sorbents for green hydrogen generation

Runxia Cai,‡<sup>a</sup> Kunran Yang,‡<sup>a</sup> Xijun Wang,‡<sup>a,b</sup> Mahe Rukh,<sup>a</sup> Azin Saberi Bosari,<sup>a</sup> Eric Giavedoni,<sup>a</sup> Alexandra Pierce,<sup>a</sup> Leo Brody,<sup>a</sup> Wentao Tang,<sup>a</sup> Phillip R. Westmoreland,<sup>a</sup> Fanxing Li\*<sup>a</sup>

Department of Chemical and Biomolecular Engineering, North Carolina State University, 911

Partners Way, Raleigh, North Carolina 27695-7905, USA

<sup>b</sup> Department of Chemical and Biological Engineering, Northwestern University, Evanston, Illinois 60208, USA

‡ These authors contributed equally to this work \*Corresponding author, fli5@ncsu.edu

Abstract:

Sorption-enhanced reforming and gasification (SERG) offers a promising approach to intensify hydrogen production from carbonaceous feedstocks. However, conventional sorbents require substantial temperature increases for the endothermic  $CO_2$  release step and are prone to deactivation. This study introduces a new class of redox-activated sorbents capable of stable isothermal operation and tunable heats of reactions, thereby facilitating an efficient reactive separation scheme. Using plane-wave density functional theory (DFT) calculations of structures and free energies, we screened 1225 perovskite-structured sorbent candidates, followed with extensive experimental validation. An effective descriptor, ( $\Delta G_{abs} + \Delta G_{reg}$ ), was identified to expedite sorbent optimization. The advanced sorbents showed reversible, isothermal carbonation of up to 78% of the A-site cation, permitting isothermal SERG or "iSERG". Their versatility was demonstrated in a fluidized bed for woody biomass gasification and a packed bed for biogas conversion, yielding hydrogen-enriched (75 vol.%) syngas from biomass and 95+% pure H<sub>2</sub> from biogas. Our results also support integrated  $CO_2$  capture to produce carbon-negative hydrogen products.

#### **Broader context**

Hydrogen is a clean energy carrier with significant potential to advance global efforts towards carbon neutrality. Among the various production methods, green hydrogen generated from sorption-enhanced reforming and gasification (SERG) of biogenic feedstocks stands out as a promising approach. However, conventional SERG technologies face critical challenges, including sorbent deactivation, substantial temperature fluctuations, and the requirement for large energy inputs to facilitate CO<sub>2</sub> release. This study

rationally designs and validates a unique family of redox-activated sorbents that are capable for isothermal CO<sub>2</sub> capture and release with excellent efficiency and stability for woody biomass and biogas conversion. Furthermore, they facilitate *in-situ* CO<sub>2</sub> capture, leading to efficient hydrogen production with negative life cycle carbon emissions. Through integration with conventional Fischer-Tropsch and methanol synthesis technologies, the isothermal SERG technology can be extended to produce carbon negative methanol and liquid fuel. Our results represent a significant advancement in sustainable hydrogen production, paving the way for broader adoption and impactful carbon reduction.

#### 1. Introduction:

Hydrogen is widely recognized as a clean-energy vector that could contribute substantially to the global effort to achieve carbon neutrality.<sup>1-3</sup> However, less than 1% of the 94 million tons of hydrogen produced in 2021 was derived from non-fossil fuel sources.<sup>4,5</sup> Given the pressing need to address global climate change and the expected growth in hydrogen demand, it is highly desirable to develop new technologies that can produce carbon-free, cost-competitive hydrogen from renewable sources.<sup>6,7</sup> Biogenic feedstocks, such as biomass and biogas, represent abundant and sustainable alternatives to coal and natural gas for hydrogen production.<sup>8-13</sup> Nevertheless, conventional gasification and reforming processes are energy-intensive, and the distributed nature of biomass and biogas sources significantly hinders the ability to leverage economies of scale. Additionally, the compositional complexity of biogenic feedstocks further inflates system complexity and costs.<sup>14-16</sup> Consequently, the development of innovative technologies that markedly intensify the hydrogen production process is essential for achieving cost-competitive renewable hydrogen generation.

Sorption-enhanced reforming and gasification (SERG) represents a promising approach to simplify hydrogen production from biogenic resources. This objective is achieved by integrating gasification/reforming, the water-gas-shift reaction, and CO<sub>2</sub> capture into a single cyclic operation. This two-step operation comprises a reforming/gasification step (with *in-situ* CO<sub>2</sub> capture) for H<sub>2</sub>-rich syngas production, followed by a decarbonation step for sorbent regeneration.<sup>17-20</sup>

Practical implementation of SERG, however, is challenged by substantial energy consumption for the decarbonation step and lack of sorbent stability over repeated cycles. Notably, all high-temperature CO<sub>2</sub> sorbents reported in the literature to date require a large temperature swing (≥100 °C) to drive the highly

endothermic  $CO_2$  release reaction ( $\Delta H = 167.6 \text{ kJ/mol}$  for  $CaCO_3$  at  $800 \,^{\circ}\text{C}$ ), a crucial condition for effective sorbent regeneration for practical applications. However, such temperature swing operations incur considerable exergy loss and thermal stress on the particles and reactors. Moreover, the prevailing CaO-based sorbents typically lose 50-80% of their initial  $CO_2$  sorption capacity after just a few dozen cycles. While steam re-activation at a lower temperature proves effective in regenerating the CaO sorbents, it introduces additional process complexity and cost. In the care of the ca

Advanced sorbents with engineered structures have also shown promise by exhibiting significantly lower deactivation rates. Nonetheless, the high cost of manufacturing these sorbents hinders their practical application, and the loss of activity, albeit slow, is generally irreversible without an additional reactivation step. Mixed oxide sorbents such as  $Ca_3Co_4O_9$  and  $Sr_{1-x}Ca_xFe_{1-y}Ni_yO_{3-\delta}$  have been explored in the context of sorption-enhanced steam reforming of glycerol. While these sorbents exhibit excellent cyclic stability through reversible phase transitions, large temperature swings are still required for the decarbonization step. Our recent study indicated that perovskite sorbents such as  $Sr_{0.25}Ba_{0.75}Fe_{0.375}Co_{0.625}O_{3-\delta}$  has the potential to operate isothermally for toluene reforming in the presence of a Ni-based reforming catalyst. Nevertheless,  $\sim 100$  °C temperature increase is still necessary for complete sorbent regeneration.

To address these challenges, this study proposes and systematically validates new families of redox-activated mixed-oxide sorbents capable of isothermal SERG (iSERG) operation with tunable heat of reaction and excellent cyclic stability. As depicted in Figure 1, a redox-active, perovskite-structured (ABO<sub>3</sub>. δ) sorbent plays a central role in this two-step process. During the reforming or gasification step, the strongly reducing environment would trigger the reduction of the B-site metal cation (e.g., Fe<sup>3/4+</sup>), which induces phase segregation. As a result, the highly basic A-site cation (e.g., Sr<sup>2+</sup>) would bind with CO<sub>2</sub> to form carbonates. In the subsequent regeneration step, the carbonated and reduced sorbent is put in contact with air or O<sub>2</sub> to trigger the oxidation of the B-site metal, leading to spontaneous release of CO<sub>2</sub> and reformation of the ABO<sub>3-δ</sub> structure. The variation in external oxygen chemical potentials would provide significantly higher thermodynamic driving force for carbonation and decarbonation reactions, when compared to temperature swings in conventional processes. Moreover, the heats for the reduction and oxidation reactions would counterbalance those of the exothermic carbonation and endothermic decarbonation reactions.

Consequently, the considerable structural and compositional flexibility of perovskite oxides, as illustrated in this study, also opens a unique avenue for tuning the thermal energy distribution between the reforming/gasification and regeneration/decarbonation steps, thereby minimizing the exergy loss for hydrogen generation.

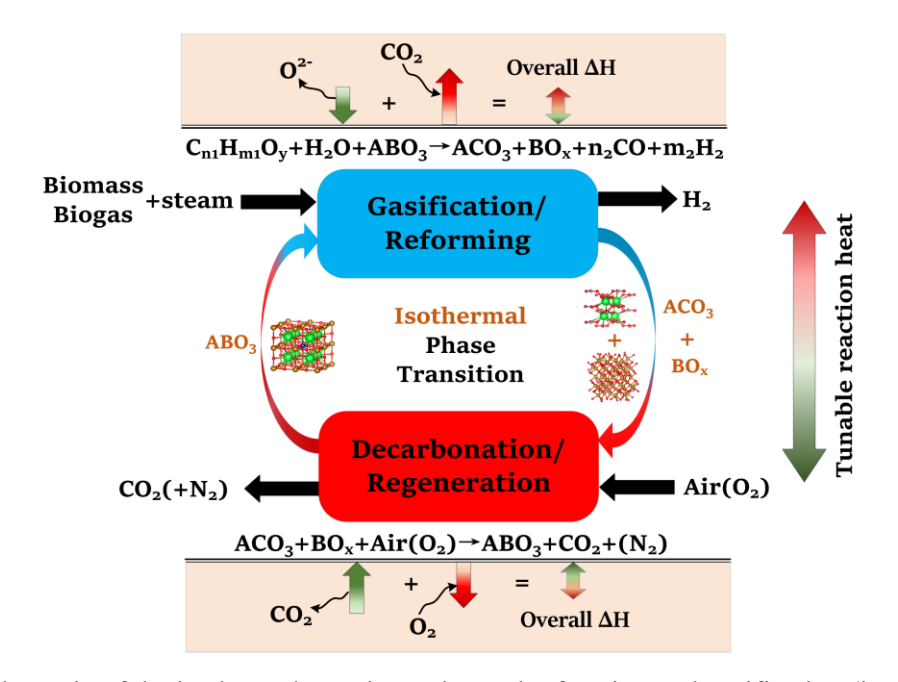


**Figure 1.** Schematic of the isothermal sorption-enhanced reforming and gasification (iSERG) concept utilizing perovskite-structured isothermal sorbents.

Taking advantage of the inherent flexibility of perovskite structures, we conducted a comprehensive screening of 1225 A/B-site doped perovskite oxides  $(Sr_xA_{1-x}Fe_yB_{1-y}O_{3-\delta})$  using plane wave density functional theory (DFT) calculations of structures and free energies. The effectiveness of our redoxactivated sorbent concept and the proposed computational framework was validated experimentally. The advanced sorbents developed in this research achieved high capacity and versatility for biomass gasification, biogas, and methane reforming. The use of concentrated  $O_2$  in the regeneration step can facilitate integrated  $CO_2$  capture, resulting in a life-cycle  $CO_2$  emission as low as -2.18 kg  $CO_2$ -eq/kg of  $H_2$ .

#### 2. Results and Discussion:

#### 2.1 High throughput computational screening

In all, 1225 sorbent compositions, with a general formula of  $Sr_xA_{1-x}Fe_yB_{1-y}O_{3-\delta}$  (A = Ca, K, or Ba and B = Mn, Ti, Co, Cu, Ni, or Mg), were considered in this study. The workflow for the computational

screening is summarized in Figure 2a. Initial steps in the workflow focus on ensuring the pre-requisites for the sorbent compositions, namely (i) charge neutrality and (ii) structural stability.

Firstly, the charge neutrality of various A and B-site cation combinations in the  $Sr_xA_{1-x}Fe_yB_{1-y}O_{3-\delta}$  structures were assessed. The total positive charge of all cations must be able to balance the total negative charge of all anions (i.e.,  $O^{2-}$ ).<sup>41</sup> Out of the initial set, 120 compositions failing to satisfy the charge neutrality criterion were excluded from further consideration, with most of these containing a large fraction of Mg ( $\geq$ 50%). Subsequently, the structural stability of the remaining perovskite compositions was investigated using the modified tolerance factor ( $\tau$ ) proposed by Bartel et al..<sup>40</sup> Derived from extensive data sets, this descriptor has demonstrated superior predictive capability for perovskite stability compared to the geometric-based Goldschmidt tolerance factor. A relaxed criterion of  $\tau$ <4.3, as reported in our recent work,<sup>41</sup> was used to screen out 230 compositions that are likely to be unstable in a perovskite structure. Many of them contained a large fraction of K on the A-site and were shown to be unstable based on our previous synthesis experience. These screening steps narrowed down the sorbent candidates to 875 compositions, summarized in Figure S1(a) (see ESI†).

Beyond structural stability, a suitable perovskite sorbent for isothermal SERG must satisfy the following criteria:

- (i) Synthesizability: the mixed oxide should be more stable than a simple mixture of its monometallic oxide precursors in an oxidizing environment (e.g., air);
- (ii) Sorption capability: the sorbent should undergo spontaneous reduction and carbonation under a reducing environment and in the presence of CO<sub>2</sub>;
- (iii) Regenerability: the sorbent should spontaneously release  $CO_2$  and reform the  $ABO_{3-\delta}$  structure under an oxidizing environment.

The reactions corresponding to these criteria are listed below. Given the reducing atmosphere in the gasifier/reformer, a Brownmillerite phase with a general formula of ABO<sub>2.5</sub> was considered in these reactions. Operational parameters compatible with actual operating conditions were used as the input parameters for the analysis. For instance, the synthesis condition was set at 1000 °C and  $P_{O2}$ =0.2 bar. The sorption step condition was 850 °C with  $P_{H2O}/P_{H2}$  = 0.2 and  $P_{CO2}$  =0.075 bar. The regeneration step condition was  $P_{O2}$  =0.2 bar and  $P_{CO2}$ =0.015 bar. We also note that these sorbent particles absorb  $P_{CO2}$  via a carbonation

# 132 H<sub>2</sub>, N<sub>2</sub>, or CH<sub>4</sub>.

$$x \text{SrO} + \frac{1 - x}{m} A_{\text{m}} O_{\text{n}} + \frac{y}{2} \text{Fe}_{2} O_{3} + \frac{1 - y}{i} B_{i} O_{j} + z_{1} O_{2} \rightarrow \text{Sr}_{x} A_{1-x} \text{Fe}_{y} B_{1-y} O_{2.5}$$
 (1)

$$Sr_{x}A_{1-x}Fe_{y}B_{1-y}O_{2.5} + CO_{2} + z_{2}H_{2} \rightarrow xSrCO_{3} + \frac{1-x}{m}A_{m}CO_{3} + \frac{y}{2}Fe_{2}O_{3} + \frac{1-y}{i}B_{i}O_{j} + z_{2}H_{2}O$$
 (2)

$$xSrCO_3 + \frac{1-x}{m}A_mCO_3 + \frac{y}{2}Fe_2O_3 + \frac{1-y}{i}B_iO_j + z_3O_2 \rightarrow Sr_xA_{1-x}Fe_yB_{1-y}O_{2.5} + CO_2$$
 (3)

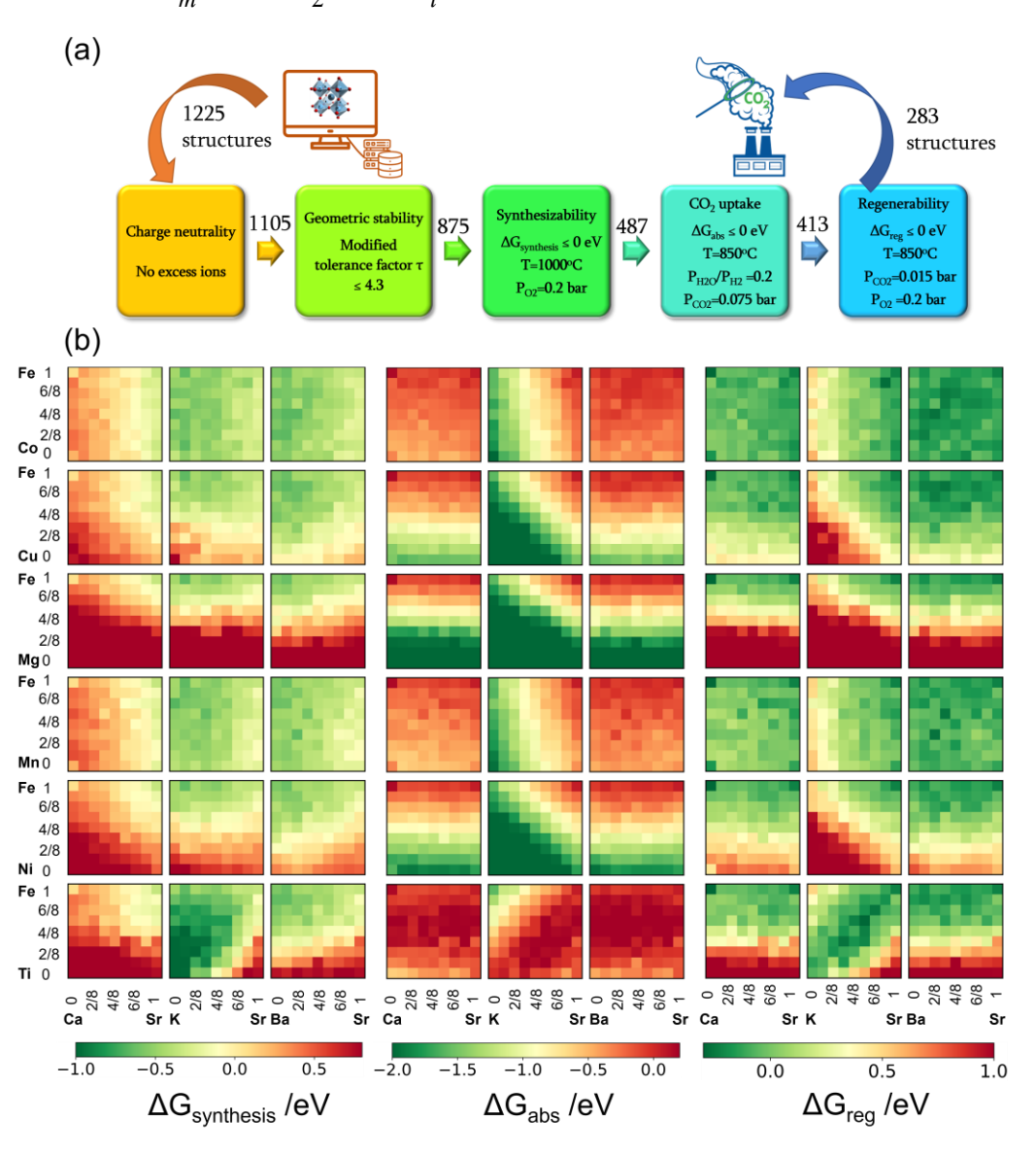


**Figure 2.** Computational screening approach and results. a) Screening workflow for iSERG sorbents. The values above each arrow represent the count of perovskite structures that successfully passed the preceding screening step. b) Heatmaps of the thermodynamic descriptors of the 1225 candidates. The values of the x and y axes denote the concentrations of Sr and Fe in Sr<sub>x</sub>A<sub>1-x</sub>Fe<sub>y</sub>B<sub>1-y</sub>O<sub>3-δ</sub>, respectively.

The Gibbs free energies of reactions 1-3, denoted as  $\Delta G_{syn(thesis)}$ ,  $\Delta G_{abs(orption)}$ , and  $\Delta G_{reg(eneration)}$ , respectively, are delineated in Figure 2b for the 875 compositions under examination. To meet the screening criteria, these  $\Delta Gs$  should be  $\leq 0$  eV to ensure adequate thermodynamic driving forces. Applying this criterion, 283 compositions were identified as potentially suitable candidates for isothermal SERG operations. Computational details, based on a combination of DFT calculations of the perovskite oxides and the bulk thermodynamic properties of both the monometallic oxides and carbonates, are provided in the methodology section. Table 1 highlights several promising sorbent composition families, whereas Figure S1e (see ESI†) summarizes all the suitable candidates predicted by the simulation. It is noted that over 90% of the SrBaFeCo and SrBaFeMn compositions were predicted to be favorable for iSERG. Therefore, our experimental investigation prioritized the SrBaFeCo and SrBaFeMn families of sorbents.

**Table 1**. Promising composition families and the corresponding dopant concentration ranges predicted by computational screening.

Compositions	General dopant concentrations at A-site and B-site	
SrBaFeMn	Ba: 0~1; Mn: 0~1	
SrBaFeCo	Ba: 0~1; Co: 0~1	
SrBaFeCu	Ba:0~1; Cu:0~0.5	
SrCaFeCo	Ca: 0~0.375; Co:0~1	
SrBaFeNi	Ba: 0~1; Ni: 0~0.375	

#### 2.2 Experimental evaluation of sorbent isothermal performance

To assess the computational screening results, 100 sorbent compositions were prepared and characterized. Among these, 80 were deemed thermodynamically suitable for iSERG applications based on the computation results. As depicted in Figure 3a and detailed in Table S1 and Figure S2 (see ESI†), X-ray diffraction (XRD) analyses revealed that 72 of the samples contained a single perovskite phase, while an additional 13 displayed minimal phase impurities. The remaining 15 samples presented at least one prominent secondary phase, although perovskite phase(s) were observed in all the samples. This confirms the effectiveness of computational screening in predicting the stability and synthesizability of the perovskite sorbents. Notably, most cobalt-containing materials, i.e.,  $Sr_xA_{1-x}Fe_yCo_{1-y}O_{3-\delta}$ , were phase-pure. This may have resulted from the flexible valence states of Co and Fe as well as the similarities in ionic radii. On the other hand, Mn-doped materials tended to segregate into two distinct perovskite phases. Ni, Mg, and Cucontaining samples also tend to phase segregate when the doping level surpassed 12.5% (1/8) on the B-site, due to their instability at a valence state above 2+. It is noted that our model estimates phase stability and synthesizability based on the relative stability of perovskite and respective monometallic oxides (Reaction 1), it does not preclude the formation of alternative, more stable mixed oxide phases.

Figure 2b displays the isothermal sorption capacities of the screened materials, defined as the percentage of A-site cations being reversibly carbonated, determined by thermogravimetric analysis (TGA). A relatively high operating temperature of 850 °C is chosen since it is commensurate with typical methane reforming and biomass gasification temperatures. This choice of operating temperature underscores an additional distinguishing feature of the redox-activated iSERG sorbents: whereas conventional sorbents are ineffective for CO<sub>2</sub> sorption at > 700 °C due to thermodynamic constraints, the iSERG sorbents do not face this limitation. This thermodynamic flexibility allows them to maintain effectiveness in the conversion of biomass and biogas. In terms of sorbent performance, it was observed that calcium doping in the A-site reduced the CO<sub>2</sub> capacity, while barium doping resulted in an increase. This trend can be explained by the instability of CaCO<sub>3</sub> at 850 °C, whereas BaCO<sub>3</sub> exhibits better stability than SrCO<sub>3</sub>. Additionally, all samples with <25% B-site doping exhibited low sorption capacity, indicating that the B-site cation

composition also plays a critical role in sorbent performance. This observation lends further credence to the proposed iSERG concept (Figure 1), emphasizing the link between the redox behavior of the B-site cations and the carbonation and decarbonation reactions. For instance, SrFeO<sub>3- $\delta$ </sub> showed a negligible (~0.13%) CO<sub>2</sub> sorption capacity, but upon doping the B-site with 75% Mn, the CO<sub>2</sub> capacity increased to 21%. Further increasing the Mn fraction to 87.5% boosted the CO<sub>2</sub> capacity to 59%. This finding aligns with DFT simulations, which revealed a decrease in  $\Delta$ G<sub>abs</sub> of 0.3 eV as Mn doping increased from 12.5% to 87.5%. More detailed fitting results (see ESI†: Figure S3(a-c)) unveiled robust correlations (R<sup>2</sup> between 0.7-0.9) between the dopant fractions of A-site and B-site elements and the CO<sub>2</sub> capacity. Additionally, doping the B-site with Ni, Mg, and Cu in amounts greater than 12.5% leads to phase segregation and are thus not suitable for iSERG.

Of all the samples tested, 21 perovskite oxides exhibited excellent sorption capacities (>35%). These high-performing sorbents primarily belong to three families: Sr<sub>x</sub>Ba<sub>1-x</sub>Fe<sub>y</sub>Co<sub>1-y</sub>O<sub>3-δ</sub>, Sr<sub>x</sub>Ca<sub>1-x</sub>Fe<sub>y</sub>Mn<sub>1-y</sub>O<sub>3-δ</sub>, and Sr<sub>x</sub>Ba<sub>1-x</sub>Fe<sub>y</sub>Mn<sub>1-y</sub>O<sub>3-δ</sub>. Among these, Sr<sub>0.75</sub>Ba<sub>0.25</sub>MnO<sub>3-δ</sub> registered the highest CO<sub>2</sub> capacity of 78%, closely followed by BaMnO<sub>3-δ</sub> and SrMnO<sub>3-δ</sub> with capacities of 77% and 75%, respectively. Within the tested Sr<sub>x</sub>Ba<sub>1-x</sub>Fe<sub>y</sub>Co<sub>1-y</sub>O<sub>3-δ</sub> samples, Sr<sub>0.625</sub>Ba<sub>0.375</sub>Fe<sub>0.5</sub>Co<sub>0.5</sub>O<sub>3-δ</sub> displayed the highest CO<sub>2</sub> capacity of ~49%. Additionally, SrFeO<sub>3-δ</sub> samples with elevated levels of cobalt doping also exhibited significant sorption capacities, such as SrCoO<sub>3-δ</sub>, which had a CO<sub>2</sub> capacity of 40%. However, the cost of cobalt may limit their economic attractiveness.

In addition to the sorption capacity, the redox-based oxygen capacity, defined as the percentage of reducible lattice oxygen removed during the gasification/reforming step, is an important parameter for redox-activated sorbents. The oxygen capacity influences (i) the overall heat of reaction for the two-step process, as the redox reaction facilitates *in-situ* combustion of a fraction of the feedstock to counterbalance the endothermic gasification or reforming processes; and (ii) the distribution of reaction heat between the two steps. Specifically, the exothermic oxidation reaction would partially offset the heat required for carbonate decomposition, while the endothermic reduction reaction mitigates heat release during the carbonation reaction. Oxygen capacities for the screened materials are depicted in Figure 3c.

Generally, within a specific sorbent family (e.g., Sr<sub>x</sub>Ba<sub>1-x</sub>Fe<sub>y</sub>Co<sub>1-y</sub>O<sub>3-δ</sub>), compositions exhibiting higher sorption capacities also tend to have higher oxygen capacities. This relationship suggests a positive correlation between the carbonation and reduction reactions, aligning with the proposed iSERG concept. Oxygen capacities are also greatly influenced by both the type and levels of dopants at the B site. For instance, materials doped with cobalt generally exhibit greater oxygen capacity than other dopants. Increasing the B-site dopant level also significantly enhanced the oxygen capacities and reducibility of the sorbents. These distinctive characteristics provide us a broad design space for choosing redox-activated CO<sub>2</sub> sorbents, allowing for the design of materials that optimally balance CO<sub>2</sub> sorption and redox properties, thereby improving iSERG performance.

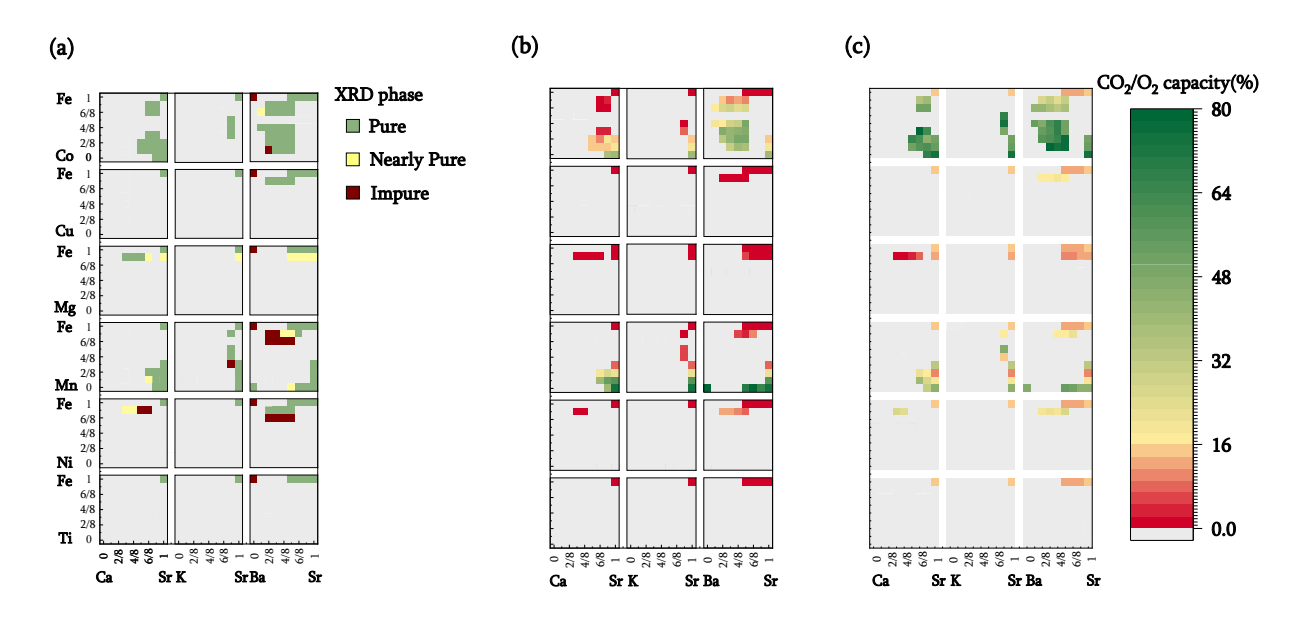


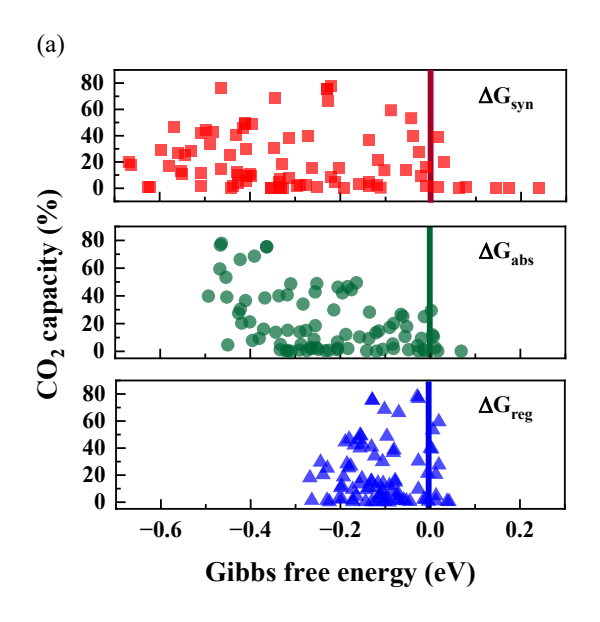
**Figure 3.** Experimental evaluation of the sorbents. a) Phase purity of the synthesized perovskites: green, yellow- and burgundy-colored cells represent pure, nearly pure, and impure samples, respectively. b) CO<sub>2</sub> sorption capacities and c) oxygen capacities of pure and nearly pure materials measured in the TGA. The rightmost color bar represents the CO<sub>2</sub> capacity for b) and the O<sub>2</sub> capacity for c).

#### 2.3 Correlating computational results and experimental performance

Although our screening method primarily focused on evaluating the thermodynamic feasibility and driving forces associated with sorption-desorption reactions, it is nevertheless instructive to explore the

correlations between experimentally measured sorption capacities and the reaction free energies predicted by DFT. Figure 4a depicts the relationships between CO<sub>2</sub> sorption capacity and various ΔGs for the 85 samples that are either pure or nearly phase-pure. Meanwhile, Figure 4b presents a confusion matrix and highlights the key parameters of the matrix to underscore the model's accuracy. Considering the potential experimental errors that can arise during CO<sub>2</sub> capacity measurement, we adopted 2% sorbent capacity as a threshold for determining thermodynamic feasibility for iSERG applications. As can be seen, the screening model achieved a precision rate of 80% and an F1 score of 0.82, confirming the effectiveness of our model and the screening criteria.

(b)



		Experiment	
		Positive	Negative
	Positive	53	13
	Negative	11	8

Accuracy: 72%; Precision: 80% Recall: 83%; F1 score: 0.82

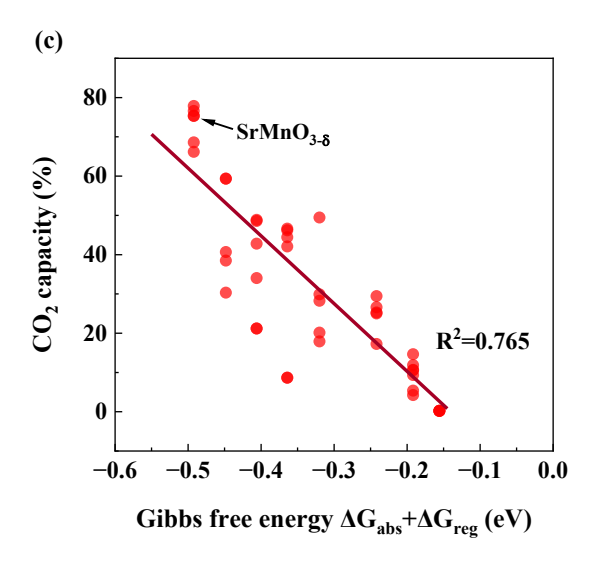


Figure 4. Correlation between computational and experimental results. a) Relationships between the CO<sub>2</sub> capacity and the different computed  $\Delta$ Gs. b) Confusion matrix and the performance of the screening model. A sample is classified as "Positive" if it exhibits a CO<sub>2</sub> capacity greater than 2%, since this confirms thermodynamic feasibility. Conversely, it is labeled as "Negative" if the capacity is less than 2%. For the prediction aspect, a "Positive" classification indicates the candidate meets all the criteria in Figure 2a and otherwise it is classified as "Negative". c) Correlation between the CO<sub>2</sub> capacity and  $\Delta$ G<sub>abs</sub>+ $\Delta$ G<sub>reg</sub> for Sr<sub>x</sub>Ba<sub>1-x</sub>Fe<sub>y</sub>B<sub>1-y</sub>O<sub>3-δ</sub> (B=Co/Mn) perovskites (40 materials total).

While predicting a sorbent's thermodynamic feasibility is crucial, identifying an effective descriptor for  $CO_2$  capacity holds greater practical value. It is therefore informative to investigate the correlation between the computationally derived thermodynamic parameters and the experimentally derived sorbent capacity. We note that  $\Delta G_{syn}$ ,  $\Delta G_{abs}$ , or  $\Delta G_{reg}$ , when used as a single fitting parameter, exhibited a weak correlation to  $CO_2$  capacity. Given the tendency for  $CaCO_3$  to decompose at the temperature of interest (850 °C) and the uncertainty related to Ca-containing solid solutions, the following fitting focused on the  $Sr_xBa_{1-x}Fe_yB_{1-y}O_{3-\delta}$  (B=Co/Mn) based materials (40 in total). Among all the fitting correlations, which are detailed in Table S2, the one involving ( $\Delta G_{abs} + \Delta G_{reg}$ ) displayed a relatively strong relationship with  $CO_2$  capacity, exhibiting a statistical  $R^2$  value of 0.765. We also note that multiple regressions provided similar correlations (Table S2). As a descriptor, ( $\Delta G_{abs} + \Delta G_{reg}$ ) also holds physical significance: materials that exhibit low ( $\Delta G_{abs} + \Delta G_{reg}$ ), which correspond to higher overall thermodynamic favorability for the

carbonation and decarbonation steps tend to exhibit higher sorption capacities. This concise descriptor can notably improve the effectiveness for sorbent optimization, since it strikes a good balance among efficiency, accuracy, and practicality. Although the current model does not consider kinetic parameters, the sorption and regeneration rates are both sufficient for efficient reforming/gasification and fast regeneration, as demonstrated in the next section.

#### 2.4 Demonstration of isothermal hydrogen generation

229

230

231

232

233

234

235

236

237

238

239

240

241

242

243

244

245

246

247

248

249

250

251

252

253

Considering its simplicity, lower raw material cost, and relative ease of scalable synthesis, we selected SrMnO<sub>3-δ</sub> for comprehensive performance evaluations. As shown in Figure 5a, SrMnO<sub>3</sub> is highly effective for iSERG of various carbonaceous feedstocks, producing ~95% pure H<sub>2</sub> from both biogas and methane, and yielding hydrogen enriched syngas with 73 vol.% H<sub>2</sub> from biomass under its more selective regime. Figure 5b shows the sorbent stability under repeated iSERG cycles using simulated biogas (CH<sub>4</sub>: $CO_2 = 2:1$ ). The XRD of reduced and regenerated samples also affirmed the reversible phase transitions (Figure S4, ESI†). Detailed data for the SrMnO<sub>3-δ</sub> sorbent with respect to the typical product gas profiles and cyclic stability with methane, biogas, and biomass are summarized in Figure S5 (see ESI†). We note that during the initial stage of the reaction, the SrMnO<sub>3-δ</sub> sorbent tends to be less selective. This is likely related to the less selective oxygen species associated with the high initial oxidation state of Mn in SrMnO<sub>3-δ</sub>. In fact, a pre-reduction of the sorbent can substantially improve selectivity (Figure S5(h), ESI†). Following a transition to SrMnO<sub>2.5</sub>, concentrated hydrogen with low CO<sub>2</sub> concentration was produced. As depicted in Figure S5(a/b) (see ESI†), even with a small sorbent bed containing 1.5 g of sorbent particles, the hydrogen production stage from methane was longer than 10 minutes, with ~95% H<sub>2</sub> purity before the CO<sub>2</sub> breakthrough. The presence of CO<sub>2</sub> in biogas accelerates the saturation of the sorbent, leading to a shorter yet still significant pre-breakthrough period (> 5 min) for hydrogen production with ~95% purity (Figure S5(c/d), ESI†). The sorbent also exhibited promising performance for biomass gasification in a fluidized bed reactor (Figure S5 (e-g), ESI†). Again, the initial stage for SrMnO<sub>3</sub> reduction was accompanied by CO<sub>2</sub> generation. This is followed by high selectivity for hydrogen generation with effective *in-situ* CO<sub>2</sub> removal.

An additional attractive feature of the iSERG is its capability for integrated CO<sub>2</sub> capture. By modulating the duration of the regeneration step with the SrMnO<sub>3</sub> sorbent, pure CO<sub>2</sub> can be produced without a breakthrough of O<sub>2</sub> (Figure S5(i/j), ESI†). For practical implementation in a circulating fluidized bed based iSERG gasifier, we anticipate a better controll over the degree of regeneration of the sorbent particles to further decrease CO<sub>2</sub> selectivity in the gasification step while producing concentrated CO<sub>2</sub> in the regeneration step. The latter is accomplished using concentrated oxygen from an air separation unit as the oxidant. This will eliminate the need for the energy-intensive CO<sub>2</sub> separation step. Sequestering the captured carbon yields a carbon-negative hydrogen product with a life-cycle global warming potential (GWP) of -2.18 kg CO<sub>2</sub>eq/kg H<sub>2</sub> (Figure 5c and Table S3, ESI†).

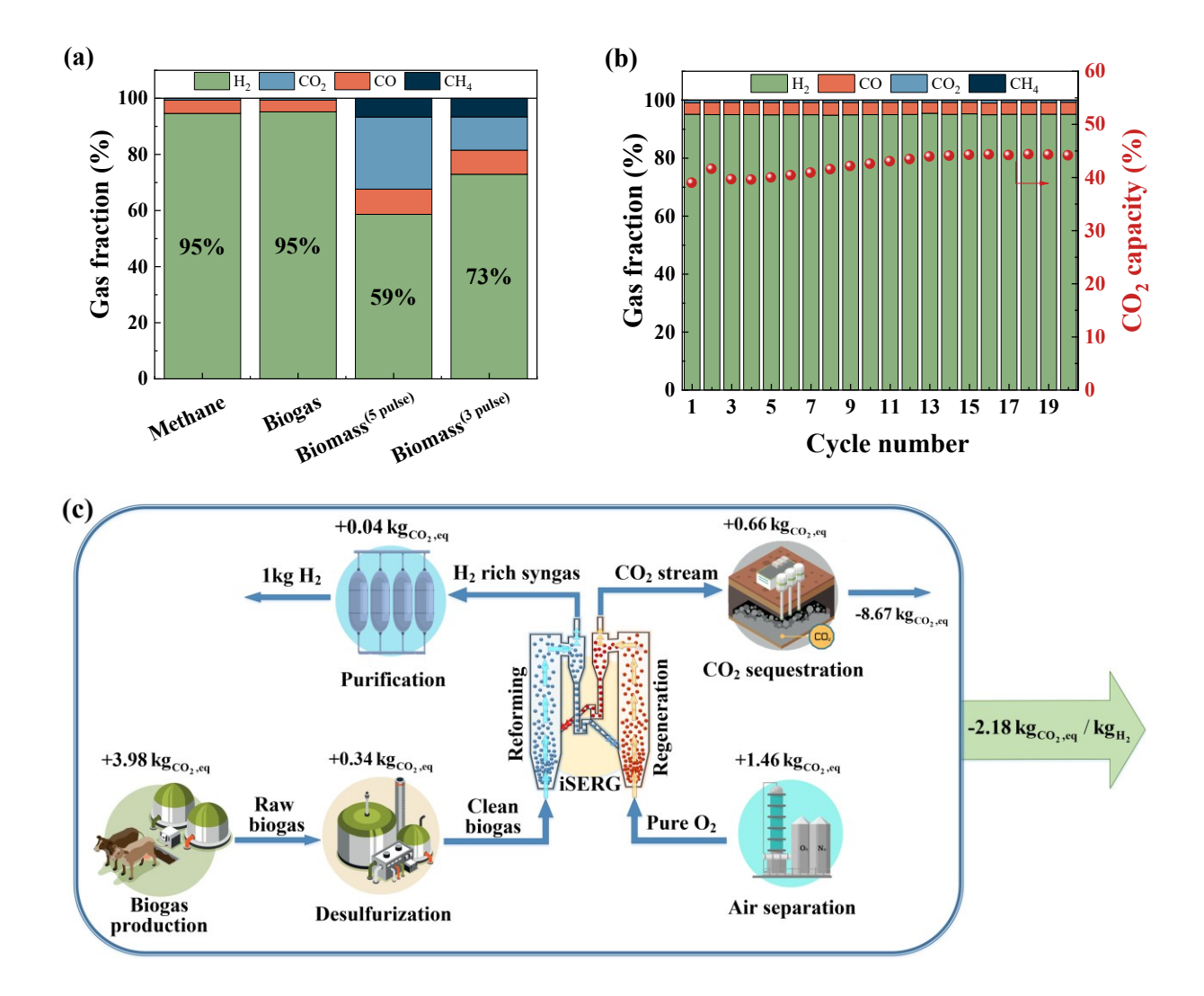


**Figure 5.** iSERG with a SrMnO<sub>3</sub> sorbent. a) product gas compositions from iSERG using methane, biogas (CH<sub>4</sub>:CO<sub>2</sub>=2:1), and biomass feedstocks. Biomass<sup>(5 pulse)</sup> represents the average gas composition of five consectuive injections of biomass samples into the fluidized bed whereas Biomass<sup>(3 pulse)</sup> represents the average gas composition from the last three injections, i.e., the more selective regime. b) Cyclic stabilty of the sorbent over 20 cycles using simulated biogas (CH<sub>4</sub>:CO<sub>2</sub>=2:1). Gas fraction is shown in a dry and Ar-free basis during the low-CO<sub>2</sub> period. c) Schematic of the life-cycle analysis (LCA) for hydrogen production via the iSERG process. The global warming potential (GWP) was calcuated based on a per kg H<sub>2</sub> basis. Recycle of the tail gas from the hydrogen purification step is not shown in this simplified schematic.

## 3. Conclusions

263

264

265

266

267

268

269

270

271

272

273

274

275

276

277

278

279

This study reports a new approach that integrates both simulation and experimental methods to engineer a unique class of perovskite-structured, redox-activated CO<sub>2</sub> sorbents. These sorbents are characterized by their stable isothermal operation and adjustable heats of reactions, enabling an efficient isothermal sorption-enhanced reforming and gasification (iSERG) process for green hydrogen production. Specifically, a high-throughput computational screening of 1225 A/B-site doped SrFeO<sub>3-8</sub> was conducted using first-principles calculations to assess their structural stability and thermodynamic favorability for iSERG. Complementary to the simulation efforts, extensive experiments were carried out to validate the effectiveness of the computation-guided sorbent design framework. Out of the 100 sorbent candidates synthesized, 85 displayed predominantly pure perovskite phases. Moreover, 80% perovskite phases predicted to be active exhibited at least 2% CO<sub>2</sub> sorption capacities. Among these, Sr<sub>0.75</sub>Ba<sub>0.25</sub>MnO<sub>3-δ</sub> demonstrated the highest CO<sub>2</sub> capacity of 78%, followed by BaMnO<sub>3-δ</sub> of 77% and SrMnO<sub>3-δ</sub> of 75%. An effective thermodynamic descriptor,  $\Delta G_{abs} + \Delta G_{reg}$ , was also identified, displaying strong correlation with the CO<sub>2</sub> capacity of sorbents. Finally, the SrMnO<sub>3-δ</sub> sorbent was extensively demonstrated for hydrogen generation through sorption-enhanced steam reforming of methane and biogas, as well as sorptionenhanced gasification of biomass. Biomass gasification in a lab-scale fluidized bed yielded nearly 75% pure H<sub>2</sub>, while both methane and biogas produced approximately 95% pure H<sub>2</sub>. This reinforces the versatility and effectiveness of the iSERG sorbents developed in this study. Our findings also support the feasibility of integrating CO<sub>2</sub> capture in iSERG to yield carbon-negative hydrogen products from biogas with a lifecycle global warming potential as low as -2.18 kg CO<sub>2</sub>eq/kg H<sub>2</sub>.

283

284

285

286

287

288

289

290

291

292

293

294

295

296

297

298

299

300

301

302

303

304

280

281

282

## 4. Experimental Section

#### 4.1 DFT calculations

Density functional theory (DFT) calculations were conducted using VASP software. 42-45 The projector-augmented wave (PAW) method was used to calculate the interaction between electrons and atomic cores. 46,47 The generalized gradient approximation (GGA) approach 48 combined with the PBE exchange-correlation functional was applied to calculate the electronic structure and corresponding energies. The cutoff energy was 450 eV. The energy threshold was set to 10<sup>-5</sup> eV and the force threshold to 0.01 eV / Å. Here spin polarization effect was considered with the initial spin moments of Co, Fe, Mn and Ni to be 5, 4, 4 and 5, respectively. In addition, and the DFT+U method was utilized to give accurate description of the d electrons for Co, Cu, Fe, Mn, Ni and Ti with the effective Hubbard U values of 3.4, 4, 4, 3.9, 6 and 3 (unit in eV).49,50 All the 2×2×1 supercell structures were built based on the brownmillerite SrFeO<sub>2.5</sub> structure. We used the Monte Carlo quasi-random structures (MCSQS) algorithm implemented in the Alloy Theoretic Automated Toolkit (ATAT) code to generate the structures under different doping conditions.<sup>51</sup> We consider the A-site dopant elements: Ba, Ca, and K, and the B-site dopant elements: Co, Cu, Fe, Mn, Ni, and Ti. It is noted that our previous work considered other A-site metals such as La, Sm, and Y. However, their carbonates are unstable at the reaction temperature of interest. These A-site elements are probably unsuitable for CO<sub>2</sub> capture under high-temperature conditions, and they are not considered in this study. For A-site and B-site doping, the doping concentrations vary from 0 to 1 with an interval of 0.125, i.e.,  $Sr_xA_{1-x}Fe_yB_{1-y}O_{2.5}$  with x and y to be 0, 0.125, ..., 0.875, and 1. By following the SQS structure generation algorithm, <sup>51</sup> 1225 Sr<sub>x</sub>A<sub>1-x</sub>Fe<sub>v</sub>B<sub>1-v</sub>O<sub>2.5</sub> structures were obtained. In addition, we further conducted vibrational

calculations for each structure and analyzed the results by using Phonopy, which could be further used to obtain free energies.<sup>52,53</sup> Similarly, calculations were performed on the metal oxides by the same procedures. Due to the complex spin state of O<sub>2</sub>, its free energies were obtained by using the CBS-QB3 method implemented in Gaussian16,<sup>54</sup> and the energies were reported before.<sup>41</sup> The other gas phase species, such as CO<sub>2</sub>, and H<sub>2</sub>O, were calculated in a cubic box with a length of 10 Å.

#### 4.2 Thermodynamic calculations

A reaction generator was developed to balance the reaction stoichiometry for the Eqs. (1-3). The Gibbs free energies of the perovskite structures and other relevant species are obtained using the methods in section 4.1. The transition between the perovskite phase and the brownmillerite phase is spontaneous under the reduction and oxidation conditions. Therefore, the brownmillerite structure was chosen as the initial state of Eq. (2) and the end state of Eq. (3) in thermodynamic analysis. This calculation approach is expected to provide more accurate results compared to using perovskites. To minimize the error arising from the inaccurate description of the free energies of species such as carbonates, experimental Gibbs free energies from HSC Chemistry software were utilized for solid reactions. These reactions include carbonation reactions (e.g.,  $SrO+CO_2 \rightarrow SrCO_3$ ) for Eq. 2, decarbonation reactions for Eq. 3, and hydrogen reduction to water for Eq. 2. The reaction free energy  $\Delta G \le 0$  eV was used as the initial criteria for Eqs. (1-3). The energies of oxides, oxygen, etc. are from DFT VASP calculations.

The first thermodynamic screening step was aligned with typical perovskite synthesis conditions ( $1000\,^{\circ}\text{C}$  and  $P_{02}$ =0.2 bar). Figure 2b presents the heatmap displaying the  $\Delta G_{\text{syn}}$  of all the structures. Notably, the stability of perovskites decreases with the increase in the doping concentrations of Cu, Mg, Ni, and Ti. However, this trend is not observed in samples doped with Co and Mn, making them more suitable for the SERG process due to their stability. A typical SERG temperature of 850  $^{\circ}\text{C}$  was selected as the reaction temperature of Eqs. 2 and 3. During the reduction/carbonation step, it is assumed that the system reaches equilibrium, with the partial pressure ratio  $P_{\text{H2O}}/P_{\text{H2}}$  set at 0.2 and  $P_{\text{CO2}}$  at 0.075 bar. During the regeneration

step, the obtained mixed metal oxides and carbonates are expected to regenerate under oxidation conditions with  $P_{O2} = 0.2$  bar and  $P_{CO2} = 0.015$  bar.

#### 4.3 Sample synthesis and characterization

329

330

331

332

333

334

335

336

337

338

339

340

341

342

343

344

345

346

347

348

349

350

351

352

353

The perovskite materials for both the screening and reactor experiments were prepared using a solidstate reaction method. For a typical synthesis of Sr<sub>x</sub>Ca<sub>1-x</sub>Fe<sub>v</sub>Co<sub>1-y</sub>O<sub>3-δ</sub> for the screening experiment in the thermogravimetric analyzer (TGA), stoichiometric amounts of SrCO<sub>3</sub>, CaCO<sub>3</sub>, Fe<sub>2</sub>O<sub>3</sub>, and Co<sub>3</sub>O<sub>4</sub> were added in a 5 ml Teflon vial and then mixed with 2 mm yttrium-stabilized ZrO2 balls with a mass ratio of 1:5. 2~3 ml ethanol (Fisher Scientific, CDA 19 (Histological)) was further added to the mixture to promote the mixing performance and reduce the particle size. A stainless-steel sample jar holding four vials with four different materials was balled milled at 1200 rpm for 3 h or 24 h using a high-energy ball mill (Vivtek Instrument: VBM-V80). The resulting wet slurry was dried in an oven at 95 °C for 30 min and 130 °C for another 30 min to remove ethanol. The dried powders were separated from ZrO<sub>2</sub> beads and then calcined at 1000 °C in a muffle furnace for 10 h to form the perovskite structure. The ramping rates for both heating and cooling steps were all set to 3 °C/min. Several Mn-doped materials were subjected to calcination at 1200 °C in a tube furnace to improve the phase purity. The fresh perovskite sorbents were sieved to two desired particle size ranges, i.e., 180-250 µm for TGA experiments and 0-180 µm for XRD. A total of 100 different materials were synthesized for the screening experiments in the TGA. A large batch of SrMnO<sub>3</sub> was prepared for the reactor experiments. The precursors were mixed in two 150 ml and two 100 ml Teflon jars and ball-milled with 3 mm, 6 mm, and 10 mm ZrO balls and then milled at 250 rpm at a 45° angel for 12 h in a planetary ball mill (Columbia International, CIT-XBM4X-2.0L). The mixture of precursor powders after the drying step was first pelletized at 20 tons before calcined at 1100 °C in the muffle furnace. Afterwards, the resulting sorbent particles were sieved into a size of 180-425 µm. The rest of the synthesis procedures were the same as the screening study. The precursors used in this study were SrCO<sub>3</sub> (Sigma Aldrich, >99.9%), CaCO<sub>3</sub> (Sigma Aldrich, >99%),

BaO (Thermo Scientific, >99.5%), Co<sub>3</sub>O<sub>4</sub> (Aldrich, >99%), Fe<sub>2</sub>O<sub>3</sub> (Noah Chemicals, >99.9%), MnO<sub>2</sub>

(Materion, >99.9 %), CuO (Noah Chemicals, >99%), KNO<sub>3</sub> (Noah Chemicals, >99%), NiO (Noah Chemicals, >99%), and MgO (Materion, >99.5%). The phase structures of the prepared fresh sorbents were characterized on a PANalytical X'Pert PRO X-ray diffraction (XRD) operating at 45 kV and 40 mA. The sample was scanned from  $2\theta$  of  $15^{\circ}$  to  $80^{\circ}$  with a step size of  $0.0262^{\circ}$  and a hold time of 0.2 s for each step. The analyses and identifications of the XRD phases of all the samples were accomplished using Highscore Plus software.

## 4.4 Experimental reactivity evaluation

354

355

356

357

358

359

360

361

362

363

364

365

366

367

368

369

370

371

372

373

374

375

376

377

378

#### TGA preliminary screening for the CO<sub>2</sub>/O<sub>2</sub> capacity

The sorption capacities of the pure and almost pure sorbents were measured in two TGAs (TA SDT Q650 and TA SDT Q600). As illustrated in Figure S7 (see ESI†), to replicate the sorption-enhanced process of carbonaceous fuels, a 4-step cycle configuration was employed, consisting of a reduction step, a regeneration step, and two purge steps before each half-cycle. During the experiments, approximately 30~50 mg of the fresh sorbents with a particle size of 180~250 µm were loaded into the TGA and then heated to 850 °C at a ramping rate of 30 °C/min under a flow of 140 SCCM Ar (Airgas UHP 5.0 grade). The gas flow rates were controlled using Alicat mass flow controllers (MC-series). Once the temperature reached 850 °C, the furnace was purged with Ar for 8 min to ensure a stable reaction temperature. Subsequently, an additional flow of 40 SCCM H<sub>2</sub> (Airgas UHP 5.0 grade) and 20 SCCM CO<sub>2</sub> (Airgas 4.0 grade) was injected for 30 min. The perovskite sorbents underwent reduction and captured CO<sub>2</sub>, leading to a noticeable weight gain. The H<sub>2</sub> and CO<sub>2</sub> gas flows were then stopped, and the furnace was purged with pure Ar for 8 min. Some of the carbonates decomposed during this step. In the subsequent 20 min regeneration step, an additional 35 SCCM O<sub>2</sub> was injected. The reduced samples were initially re-oxidized and gained some weight in the first 1~2 min, followed by the release of a significant amount of CO<sub>2</sub>. Afterward, the first cycle was accomplished, and an identical second cycle was initiated. The CO<sub>2</sub> capacity was determined by measuring the weight changes in the second cycle. However, certain perovskites exhibited limited kinetics, preventing complete regeneration within the 20 min timeframe. In order to

ascertain the oxygen non-stoichiometry at the complete oxidation conditions, these perovskite materials were subjected to 850 °C under 20% O<sub>2</sub> atmosphere. Additionally, a reference point was established for each material by reducing the perovskite at 1100 °C in a 20% H<sub>2</sub> atmosphere, leading to a complete transformation to a mixture of pure metals and metal oxides. The CO<sub>2</sub> capacity was defined as the measured molar amount of CO<sub>2</sub> absorbed compared to the theoretical molar amount of CO<sub>2</sub> absorbed by A-site elements. The O<sub>2</sub> capacity was defined as the measured molar amount of released O atoms compared to the molar amount of the sorbent. Further details about the calculation approach can be found in the ESI†.

#### Sorption-enhanced steam reforming of methane and biogas in a packed bed

379

380

381

382

383

384

385

386

387

388

389

390

391

392

393

394

395

396

397

398

399

400

401

402

403

The sorption-enhanced steam reforming of methane and biogas was demonstrated in a quartz U-tubepacked bed with a 6 mm inner diameter. As illustrated in Figure S8 (see ESI†), a sequential bed configuration was utilized to achieve a high methane conversion. 0.3 g of nickel-based steam reforming catalysts (Alfa Aesar, HiFUEL R110) was utilized in the upstream section, and 1.5 g of sorbents were employed in the downstream section. Both the catalyst and sorbent particles were sieved to a size range of 180 to 425 µm. Quartz wool and SiC were used as inert packing material to prevent blowout and preheat the inlet gas. The reactor was heated to 850 °C at a ramping rate of 30 °C/min and then sustained at 850 °C throughout the entire experiment. A typical 4-step cycle configuration was also adopted, i.e., a 20 min purge step, a 20 min reduction step, another 10 min purge step, and a 20 min regeneration step. A flow of 30 SCCM Ar (Airgas UHP 5.0 grade) was maintained as the carrying gas throughout the entire cycle. For the methane reforming scenario, a flow of 5 SCCM CH<sub>4</sub> (Airgas UHP 5.0 grade) was introduced during the reduction step along with 7.35 μL/min of deionized water regulated by a syringe pump. This corresponded to a steam-to-carbon molar ratio of 2. For the biogas reforming scenario, a flow of 5 SCCM CH<sub>4</sub> (Airgas UHP 5.0 grade) was cofed with 2.5 SCCM CO<sub>2</sub> (Airgas UHP 4.5 grade) alongside the continuous infusion of 7.35 µL/min of deionized water. The water was injected 3 min prior to methane injection, ensuring a stable steam flow rate at the onset of the reduction step. During the regeneration step, 7.5 SCCM of O<sub>2</sub> (Airgas extra dry grade) was injected to create a 20% O<sub>2</sub> atmosphere.

To mitigate the less selective regime, another experiment was implemented with the incorporation of a pre-reduction step. The sample was pre-reduced with a gas mixture of 6 SCCM H<sub>2</sub> and 30 SCCM Ar for 10 min, followed by an Ar purge prior to the normal reaction cycle. Additionally, another experiment aimed at producing pure CO<sub>2</sub> without O<sub>2</sub> breakthrough for sequential carbon capture involved a shortened regeneration time. To control the reaction environment, 1.75 g sorbents, 4 SCCM of CH<sub>4</sub>, 2.3 SCCM of CO<sub>2</sub>, 5.88 μL/min of deionized water, and an 8 min regeneration time were utilized. The methane-to-carbon dioxide ratio was adjusted to match a typical biogas composition in the literature.<sup>55</sup> Throughout these experiments, steam was condensed and separated downstream, and the remaining gaseous products were analyzed using an MKS Cirrus II quadrupole mass spectrometer (QMS). The reduced and regenerated samples from the biogas experiments were collected and tested using XRD to validate the reversibility for phase transition. Due to mass transfer limitations in the pack bed, the regenerated samples taken from the reactors were treated in TGA at 850°C under a continuous flow of 40 SCCM O<sub>2</sub> and 160 SCCM Ar prior to XRD characterization.

#### Sorption-enhanced gasification of biomass in a fluidized bed

The performance of SrMnO<sub>3</sub> for sorption-enhanced gasification of biomass was demonstrated in a laboratory-scale bubbling fluidized bed reactor. As shown in Figure S9 (see ESI†), a vertical 304# stainless steel tube with a 25.4 mm outer diameter (OD) and 23.6 mm inner diameter (ID) was used as the reactor. The reactor was housed in a tube furnace (MTI OTF-1200X-S-VT) with a heating zone of around 20 cm. The furnace thermocouple (S-type), located in the middle of the heating zone, serves as the reference for the reaction temperature. Prior to the experiment, the bottom of the reactor tube was loaded with 16 mesh Al<sub>2</sub>O<sub>3</sub> to support the sorbents. Subsequently, 15 g SrMnO<sub>3</sub> was loaded into the reactor, corresponding to a static bed height of approximately 2 cm. A typical 4-step cycle configuration was adopted, comprising of a reduction step, a regeneration step, and a purge step between each half-cycle. 923 SCCM Ar (Airgas, UHP 5.0) was injected during the reduction and purge steps, while a mixture of 683 SCCM Ar/240 SCCM O<sub>2</sub> was injected during the regeneration step. The gas flow rates were controlled by mass flow controllers (Brooks, 5850 E series). Water was injected through a 3.18mm OD x 1.76 mm ID stainless steel tube

inserted into the heating zone. The temperature in the heating zone greatly surpassed the boiling point of the water, thereby ensuring vaporization of water into steam. The volumetric flow rate of water, controlled by a syringe pump (Harvard Apparatus), was set to 0.21 ml/min, corresponding to 277 SCCM and a steamto-Ar molar ratio of 0.3. The product gas stream was heat-traced before flowing through a flask submerged in ice water to condense the steam in the effluent and tar (if present). The effluent gas stream was then sent to an MKS Cirrus II quadrupole mass spectrometer to determine the gas compositions. For biomass injection into the reactor, a 3.75mm OD/3.35 mm ID stainless steel tube was used. The lower end of the tube was inserted into the center of the sorbent bed to enhance the mixing of sorbents and biomass. A pulse injection mode was employed, where ~0.3g of pulverized pine wood (200 to 500 μm) was first loaded into the top part of the tube, and then around 3 ml helium gas at 25 PSIG pressure was utilized to carry the biomass powder into the reactor. A second gas injection was performed subsequently to prevent any residual biomass from being stuck in the tubing. Five pulse injections of biomass were conducted for each cycle, and four cycles were conducted to achieve a stable sorption-enhanced performance for syngas production. The ultimate and proximate analyses of the biomass feedstock are listed in Table S4. The CO<sub>2</sub> capacity was also defined as the measured molar amount of CO<sub>2</sub> released in the regeneration step compared to the theoretical molar amount of CO2 absorbed by A-site elements. The cold gas efficiency was defined as the produced gas calorific value with respect to the low heating value of biomass.

447

448

449

450

453

430

431

432

433

434

435

436

437

438

439

440

441

442

443

444

445

446

## **Supplementary Information**

Electronic supplementary information (ESI) † is available online.

## Data and code availability

The data supporting the findings are available within the main text and ESI†. More detailed data can be

452 made available upon request.

## **Author contributions**

- Conceptualization, F.L.; methodology, R.C., K.Y., X.W., F.L.; investigation, R.C., K.Y., X.W., M.R., A.-
- S.B., E.G., A.P., L.B., W.T.; writing original draft, R.C., K.Y.; writing review & editing, R.C., K.Y.,
- X.W., L.B., W.T., P.W., F.L.; funding acquisition, F.L.; resources, F.L.; supervision, F.L..

## 457 **Conflict of Interest**

459

467

468

The authors declare no conflict of interest.

## Acknowledgements

- 460 This work was supported by the U.S. Department of Energy Office of Energy Efficiency & Renewable
- Energy (no. EE0008809) and the US National Science Foundation (CBET-1923468). We acknowledge the
- use of the Analytical Instrumentation Facility (AIF) at North Carolina State University, which is supported
- by the State of North Carolina and the National Science Foundation. We also acknowledge the computing
- 464 resources provided by North Carolina State University High Performance Computing Services Core
- 465 Facility (RRID:SCR 022168). We also thank Dr. Fan Yang and Dr. Yuan Yao (Yale University) for their
- suggestions with respect to the life-cycle analysis.

#### References

- 469 1 C. Acar, I. Dincer, *Int. J. Hydrogen Energy* **2020**, *45* (5), 3396-3406.
- 470 2 T. da Silva Veras, T. S. Mozer, D. da Costa Rubim Messeder dos Santos, A. da Silva César, *Int. J. Hydrogen Energy* **2017**, *42* (4), 2018-2033.
- 472 3 M. Yue, H. Lambert, E. Pahon, R. Roche, S. Jemei, D. Hissel, *Renew. Sust. Energ. Rev.* **2021**, *146*, 473 111180.
- 474 4 International Energy Agency, Global hydrogen review 2022, Paris, https://www.iea.org/reports/global-hydrogen-review-2022. (Access. May. 6<sup>th</sup>, 2024); 2022.
- 476 5 A. Zapantis, Circular carbon economy series: blue hydrogen., Apr. 2021. 477 https://www.globalccsinstitute.com/wp-content/uploads/2021/04/Circular-Carbon-Economy-series-
- Hue-Hydrogen.pdf (Access. May 6<sup>th</sup>, 2024).
- 479 6 N. Sazali, Int. J. Hydrogen Energy **2020**, 45 (38), 18753-18771.
- 480 7 F. Dawood, M. Anda, G. M. Shafiullah, *Int. J. Hydrogen Energy* **2020**, *45* (7), 3847-3869.
- 481 8 L. Cao, I. K. M. Yu, X. Xiong, D. C. W. Tsang, S. Zhang, J. H. Clark, C. Hu, Y. H. Ng, J. Shang, Y. S. Ok, *Environ. Res.* **2020**, *186*, 109547.
- 483 9 V. S. Sikarwar, M. Zhao, P. Clough, J. Yao, X. Zhong, M. Z. Memon, N. Shah, E. J. Anthony, P. S. Fennell, *Energy Environ. Sci.* **2016**, *9* (10), 2939-2977.
- 485 10 U.S. Department of Energy. DOE national clean hydrogen strategy and roadmap, Jun. 2023.
- https://www.hydrogen.energy.gov/library/roadmaps-vision/clean-hydrogen-strategy-roadmap
- 487 (Access May 6<sup>th</sup>, 2024).

- 488 11 X. Zhao, H. Zhou, V. S. Sikarwar, M. Zhao, A.-H. A. Park, P. S. Fennell, L. Shen, L.-S. Fan, *Energy Environ. Sci.* **2017**, *10* (9), 1885-1910.
- 490 12 Y. Gao, J. Jiang, Y. Meng, F. Yan, A. Aihemaiti, Energy Convers. Manage. 2018, 171, 133-155.
- T. Mendiara, F. García-Labiano, A. Abad, P. Gayán, L. F. de Diego, M. T. Izquierdo, J. Adánez, *Appl. Energy* 2018, 232, 657-684.
- 493 14 J. Andersson, J. Lundgren, *Appl. Energy* **2014**, *130*, 484-490.
- 494 15 Y. Richardson, J. Blin, A. Julbe, *Prog. Energy Combust. Sci.* **2012**, *38* (6), 765-781.
- 495 16 M. Puig-Gamero, J. Argudo-Santamaria, J. L. Valverde, P. Sánchez, L. Sanchez-Silva, *Energy Convers. Manage.* **2018**, *177*, 416-427.
- 497 A. M. Parvez, S. Hafner, M. Hornberger, M. Schmid, G. Scheffknecht, *Renew. Sust. Energ. Rev.* **2021**, 498 *141*, 110756.
- 499 18 D. Chen, L. He, *ChemCatChem* **2011**, *3* (3), 490-511.
- 500 19 M. Broda, A. M. Kierzkowska, D. Baudouin, Q. Imtiaz, C. Copéret, C. R. Müller, *ACS Catal.* **2012**, 2 (8), 1635-1646.
- 502 20 C. Dang, L. Liu, G. Yang, W. Cai, J. Long, H. Yu, Chem. Eng. J. 2020, 383, 123204.
- 503 21 J. Udomsirichakorn, P. Basu, P. Abdul Salam, B. Acharya, Fuel Process. Technol. 2014, 127, 7-12.
- 504 22 H. An, T. Song, L. Shen, C. Qin, J. Yin, B. Feng, *Int. J. Hydrogen Energy* **2012**, *37* (19), 14195-505 14204.
- 506 23 B. Jiang, B. Dou, K. Wang, C. Zhang, M. Li, H. Chen, Y. Xu, Chem. Eng. J. 2017, 313, 207-216.
- 507 24 J. C. Abanades, Chem. Eng. J. 2002, 90 (3), 303-306.
- 508 25 F. D. M. Daud, K. Vignesh, S. Sreekantan, A. R. Mohamed, New J. Chem. 2016, 40 (1), 231-237.
- 509 26 G. S. Grasa, J. C. Abanades, *Ind. Eng. Chem. Res.* **2006**, *45* (26), 8846-8851.
- 510 27 V. Manovic, E. J. Anthony, Environ. Sci. Technol. 2007, 41 (4), 1420-1425.
- 511 28 H. K. Rusten, E. Ochoa-Fernández, H. Lindborg, D. Chen, H. A. Jakobsen, *Ind. Eng. Chem. Res.* 512 **2007,** 46 (25), 8729-8737.
- 513 29 H. R. Radfarnia, M. C. Iliuta, Chem. Eng. Process. 2014, 86, 96-103.
- 514 30 G. Wu, C. Zhang, S. Li, Z. Huang, S. Yan, S. Wang, X. Ma, J. Gong, *Energy Environ. Sci.* **2012**, *5* (10), 8942.
- 516 31 A. Armutlulu, M. A. Naeem, H. J. Liu, S. M. Kim, A. Kierzkowska, A. Fedorov, C. R. Muller, *Adv. Mater.* **2017**, *29* (41), 1702896.
- 518 32 M. T. Dunstan, F. Donat, A. H. Bork, C. P. Grey, C. R. Muller, *Chem Rev* **2021**, *121* (20), 12681-12745.
- 520 33 V. Manovic, E. J. Anthony, Fuel **2011**, 90 (1), 233-239.
- 521 34 F.-C. Yu, N. Phalak, Z. Sun, L.-S. Fan, *Ind. Eng. Chem. Res.* **2011**, *51* (4), 2133-2142.
- 522 35 H. Sun, J. Wang, J. Zhao, B. Shen, J. Shi, J. Huang, C. Wu, *Appl. Catal. B: Environ.* **2019,** 244, 63-523 75.
- 524 36 L. Brody, R. Cai, A. Thornton, J. Liu, H. Yu, F. Li, ACS Sustain. Chem. Eng. **2022**, 10 (19), 6434-525 6445.
- 526 37 C. Dang, Y. Li, S. M. Yusuf, Y. Cao, H. Wang, H. Yu, F. Peng, F. Li, *Energy Environ. Sci.* **2018**, *11* 527 (3), 660-668.
- 528 38 C. Dang, H. Yu, H. Wang, F. Peng, Y. Yang, Chem. Eng. J. 2016, 286, 329-338.
- 529 39 L. Brody, M. Rukh, R. Cai, A. Saberi Bosari, R. Schomäcker, F. Li, *J. Phys. Energy* **2023**, *5* (3), 035004.
- 531 40 C. J. Bartel, C. Sutton, B. R. Goldsmith, R. Ouyang, C. B. Musgrave, L. M. Ghiringhelli, M. Scheffler, 532 *Sci Adv* **2019**, *5* (2), eaav0693.
- 533 41 X. Wang, Y. Gao, E. Krzystowczyk, S. Iftikhar, J. Dou, R. Cai, H. Wang, C. Ruan, S. Ye, F. Li, 534 Energy Environ. Sci. 2022, 15 (4), 1512-1528.
- 535 42 G. Kresse, J. Furthmüller, *Comput. Mater. Sci.* **1996**, *6* (1), 15-50.
- 536 43 G. Kresse, J. Furthmuller, *Phys Rev B Condens Matter* **1996**, *54* (16), 11169-11186.
- 537 44 G. Kresse, J. Hafner, *Phys Rev B Condens Matter* **1993**, 47 (1), 558-561.
- 538 45 G. Kresse, J. Hafner, *Phys. Rev. B* **1994**, *49* (20), 14251-14269.

- 539 46 P. E. Blochl, *Phys Rev B Condens Matter* **1994**, *50* (24), 17953-17979.
- 540 47 G. Kresse, D. Joubert, *Phys. Rev. B* **1999**, *59* (3), 1758-1775.
- 541 48 J. P. Perdew, K. Burke, M. Ernzerhof, *Phys. Rev. Lett.* **1996**, 77 (18), 3865-3868.
- 542 49 A. Jain, G. Hautier, C. J. Moore, S. Ping Ong, C. C. Fischer, T. Mueller, K. A. Persson, G. Ceder,
   543 Comput. Mater. Sci. 2011, 50 (8), 2295-2310.
- 544 50 G. Hautier, S. P. Ong, A. Jain, C. J. Moore, G. Ceder, *Phys. Rev. B* **2012**, *85* (15), 155208.
- 545 51 A. van de Walle, P. Tiwary, M. de Jong, D. L. Olmsted, M. Asta, A. Dick, D. Shin, Y. Wang, L. Q. Chen, Z. K. Liu, *Calphad* **2013**, *42*, 13-18.
- 547 52 A. Togo, J. Phys. Soc. Jpn. **2023**, 92 (1), 012001.
- 548 53 A. Togo, I. Tanaka, Scripta Mater. 2015, 108, 1-5.
- 549 54 M. J. Frisch, G. W. Trucks, H. B. Schlegel, G. E. Scuseria, M. A. Robb, J. R. Cheeseman, G. Scalmani, V. Barone, G. A. Petersson, H. Nakatsuji, X. Li, M. Caricato, A. V. Marenich, J. Bloino, B. G. Janesko.
- V. Barone, G. A. Petersson, H. Nakatsuji, X. Li, M. Caricato, A. V. Marenich, J. Bloino, B. G. Janesko, R. Gomperts, B. Mennucci, H. P. Hratchian, J. V. Ortiz, A. F. Izmaylov, J. L. Sonnenberg, Williams,
- F. Ding, F. Lipparini, F. Egidi, J. Goings, B. Peng, A. Petrone, T. Henderson, D. Ranasinghe, V. G.
- Zakrzewski, J. Gao, N. Rega, G. Zheng, W. Liang, M. Hada, M. Ehara, K. Toyota, R. Fukuda, J.
- Zakizewski, J. Gao, N. Rega, G. Zheng, W. Liang, W. Hada, W. Ehara, K. Toyota, K. Fukuda, J.
- Hasegawa, M. Ishida, T. Nakajima, Y. Honda, O. Kitao, H. Nakai, T. Vreven, K. Throssell, J. A.
- Montgomery Jr., J. E. Peralta, F. Ogliaro, M. J. Bearpark, J. J. Heyd, E. N. Brothers, K. N. Kudin, V.
- N. Staroverov, T. A. Keith, R. Kobayashi, J. Normand, K. Raghavachari, A. P. Rendell, J. C. Burant,
- 557 S. S. Iyengar, J. Tomasi, M. Cossi, J. M. Millam, M. Klene, C. Adamo, R. Cammi, J. W. Ochterski,
- R. L. Martin, K. Morokuma, O. Farkas, J. B. Foresman, D. J. Fox *Gaussian 16 Rev. C.01*, Wallingford, CT, 2016.
- 560 55 N. Hajjaji, S. Martinez, E. Trably, J.-P. Steyer, A. Helias, *Int. J. Hydrogen Energy* **2016**, *41* (14), 6064-6075.